Applied Magnetic Resonance (2022) 53:417–439
https://doi.org/10.1007/s00723-021-01456-6

Applied
Magnetic Resonance

ORIGINAL PAPER

Quantitative Evaluation of Phase Distribution in UHMWPE as Derived from a Combined Use of NMR FID Analysis and Monte Carlo Simulation

Eddy Hansen[1] · **Alireza Hassani**[1,2]

Received: 23 September 2021 / Revised: 24 November 2021 / Accepted: 26 November 2021 /
Published online: 6 December 2021

Abstract
A new and robust statistical approach is explored with the objective to derive quantitative and reliable information on the molecular dynamics within distinct domains (crystalline, intermediate and amorphous domains) of ultra-high molecular weight polyethylene (UHMWPE). The method consists of a critical evaluation of the free induction decay (FID) model, which is used to generate synthetic FID with a predefined signal-to-noise ratio by Monte Carlo simulations. The application of the method is demonstrated for three UHMWPE samples. A subsequent model fitting of their synthetic FIDs revealed a unique correlation between the error, i.e., standard deviation, of the derived parameters and the FID signal-to-noise ratio (SNR_{FID}). Moreover, it was found that the method can be used to estimate the minimum required sampling time to obtain reliable parameter estimation of the FID model to experimental data.

1 Introduction

Polyethylene (PE) possesses a semi-crystalline complex topology composed of crystalline and disordered amorphous regions. The heterogeneous structure of PE in solid-state enables a diverse range of mechanical and transport properties. The interdependence between structure and physical properties of ultra-high molecular weight polyethylene (UHMWPE) becomes even more significant in the solid, semi-crystalline state for molecular weight exceeding 10^6 g/mol. This increase in significance is due to the entanglements, defined as a steric hindrance between (long) chains, in the amorphous region. The existing literature noted that the

✉ Eddy Hansen
e.w.hansen@kjemi.uio.no

[1] Department of Chemistry, University of Oslo, Blindern, P. O. Box 1033, 0315 Oslo, Norway

[2] Norner Research AS, Asdalstrand 291, 3962 Stathelle, Norway

entanglements in the amorphous region limit the mechanical properties of UHMWPE [1, 2].

Additionally, any change in morphology due to the thermal and mechanical processing pathways may affect the crystallinity and the chain dynamics within the different regions of such materials [3–5]. This means that the relationship between structure and material properties of UHMWPE is an important issue when exploring the emerging and accelerating area of applications of such high-performance materials. Hence, an improved characterization of the crystalline- and non-crystalline phases and their regional mobilities provide invaluable insight into the morphological properties of UHMWPE prepared under different processing conditions.

Differential scanning calorimetry (DSC), X-ray scattering, and density measurements are commonly used to estimate the mass or volume fraction of the crystalline phase. However, these methods are mainly based on indirect observations and quantification of crystalline regions. As a result, information on the interphase located between the crystalline domain and the amorphous region is more challenging to obtain. In contrast, nuclear magnetic resonance is an alternative experimental technique to probe semi-crystalline materials, as all domains and their dynamics are detected simultaneously.

Both ^{1}H- and ^{13}C-NMR have been frequently applied to investigate the crystalline/amorphous regions in PE. For an accurate quantitative determination of crystalline- and non-crystalline domains in PE. ^{1}H-NMR is an exciting option due to the inherently short proton spin–lattice relaxation times (T_1 relaxation), as compared to ^{13}C NMR. In our previous quantitative study, a recycle time of approximately 2000s was required in ^{13}C NMR, while a corresponding recycle time of less than 2–6 s was acquired in ^{1}H NMR [6]. We further demonstrated that the low-field NMR instruments can deliver consistent results comparable to high-field spectrometers. Therefore, in this study, we chose to conduct the characterization at a low field to investigate the capability of such commercially emerging spectrometers.

Low-field NMR instruments are gaining increasing attention, as this class of instruments is robust, less costly, and easier to handle than high-field NMR spectrometers [7, 8]. Fortunately, there are reasonable theoretical arguments that the observed ^{1}H-FID of PE can be resolved to give detailed information regarding the different phases or domains: crystalline, intermediate and amorphous. As a result, a number of semi-empirical relaxation models have been developed and applied successfully to resolve the time domain signal (FID) into its respective phase components [9, 10]. However, compared to high-field NMR spectrometers, a low-field NMR instrument typically suffers from a much poorer signal-to-noise ratio (SNR), which affects the quality of the data obtained by model fitting (of the FID).

A frequently asked question is whether the NMR characteristics (phase distribution and relaxation time characteristics) derived by model fitting the FID of two different samples are significantly different or not. For example, if the derived NMR characteristics (including error) of one sample are known, what is the minimum number of scans needed to acquire an FID of a second sample to ensure that the derived NMR characteristics of the latter sample are significantly different (within a 95% confidence interval) from the former?

Hence, a novel approach is presented and discussed to extract quantitative and reliable information on the distribution and molecular dynamic features within the crystalline, intermediate and amorphous domains of UHMWPE. The main topic in this work will be dedicated to the model fitting of both experimental and synthetic FIDs of typical UHMWPE samples, with the objective to explore the reproducibility and inherent error (95% confidence interval) in the derived domain fractions (crystalline, intermediate and amorphous domains) and their corresponding relaxation time characteristics. For this purpose, we have explored three samples exposed to significantly different processing conditions.

2 Experimental Section

2.1 Materials

Three ultra-high-molecular-weight samples of polyethylene (UHMWPE), designated C, MC, and SC, were investigated.

C: Commercial sample (grade name: GUR4120) was purchased from Celanese having an average molecular weight of 4700 kg/mol (as estimated based on its intrinsic viscosity, using Margolis's equation) according to the supplier. The polymer sample was a powder and was used as received.

MC: Commercial sample (grade name: GUR4120) that was melt crystallized and compression molded (COLLIN P300P) initially at 180 °C under 5 bars for 300 s. Then the pressure was increased to 50 bars and kept for 900 s. After the run, the sample was rapidly cooled down to room temperature (> 30 °C/min).

SC: Commercial sample (trademark: GUR410) crystallized from xylene (isomeric mixture, VWR chemicals) at a fixed polymer concentration of 0.5 wt%. The polymer was dissolved at 135 °C, and the solution was kept at the said temperature for 2 h before being cast in an aluminum tray. Upon cooling, it was visually observed that the solution turned into a gel that was kept in a fume hood at room temperature for 12 h and thereafter at room temperature in a chamber under reduced pressure 200 mbar for 7 days under with constant air purging.

2.2 Experimental Methods and Procedures

A commercial, time-domain ^{1}H-NMR instrument operating at 0.47 Tesla and denoted AMR R4 or Antek R4 was used throughout this work. The temperature was fixed at (60.0 ± 0.5) °C and the sample equilibrated for 10 min before onset of any experiment. The 90° pulse was set to 1.5 μs and the FID acquired with a fixed dwell time of 1 μs. The probe dead time was fixed at 5.0 μs with a first sampling point acquired at 5.75 μs. Each sample was packed into a 10 mm (outer diameter) NMR tube and filled up to a height of 10 mm before placed into the most homogeneous part of the magnet. This is to minimize the effect of rf-inhomogeneity and inherent magnetic field heterogeneities as well as magnetic field inhomogeneities arising from an inhomogeneous magnetic susceptibility of heterogeneous samples. The B_0

heterogeneity was of the order of 1 kHz and the Rf-inhomogeneity was less than 6% within the 1 cm^3 sample volume.

For instance, the FID of bulk water revealed a systematically smaller intensity compared to the CPMG decay for times longer than approximately 150 µs. Hence, distortion-less FIDs were only obtained within an acquisition window of between 0 and 150 µs.

In addition, the filling factor between samples differed, causing the signal-to-noise ratio (SNR_{FID}) of their respective FID to differ, as well (when acquired with the same number of scans). The number of scans (NS) was varied systematically between 250 and 4096.

Spin–lattice relaxation time (T_1) was determined using a saturation recovery (90°-τ-90°) pulse sequence with 30 τ-values and 64 scans. The repetition time between pulses was set to a value of between 4 and 5 times the maximum T_1 to ensure quantitative sampling.

Spin–spin relaxation times and component fractions were determined by model fitting the FID using a non-linear least squares (NLLS) technique combined with the Levenberg–Marquardt algorithm (Origin, version 2020, OriginLab Corporation, Northampton, MA, USA).

Signal-to-noise ratio of the FID—denoted SNR_{FID}—is calculated from Eq. (1) and represents the main and critical parameter in this work.

$$SNR_{FID} = I_0/\sigma_{FID}, \tag{1}$$

where I_0 represents the signal intensity of the FID at the start of the acquisition and σ_{FID} defines the standard deviation of the noise in the signal free tale of the FID, which was composed of more than 400 data points. Notably, each FID was baseline corrected before model fitting.

Synthetic FIDs were generated by Monte Carlo simulations (Excel/Excel 2016) and subsequently model-fitted by a predefined FID model using a non-linear-least-squares technique (Origin, version 2020).

2.3 Bayesian Information Criterion (BIC) Number

Bayesian Information Criterion (BIC) number is a statistical parameter and defined according to Eq. (2) [11]:

$$BIC = n \ln\left(\frac{RSS}{n}\right) + k \ln(n), \tag{2}$$

where k is the number of model parameters, n is the number of data points, and RSS is the residual sum of squares between observed and model calculated data. When comparing two different models, the model with the smaller BIC number is the best if the difference (ΔBIC) between their respective BIC numbers is larger than about two (2). For $\Delta BIC < 2$, the two models are not significantly different. However, the model with the least number of adjustable parameters is normally chosen by convention.

3 Theory

3.1 FID Model

The choice of a representative FID model is of crucial importance and is elaborated in this section.

A semi-crystalline polymer can be considered composed of three major domains: a crystalline- (C), an intermediate- (I), and an amorphous domain (A), with a distribution characterized by their relative intensities I_C, I_I, and I_A, respectively. Each domain is assigned a single (average) spin–spin relaxation time: T_{2C}, T_{2I}, and T_{2A}, which gives insight into the molecular dynamics within the respective domain. Since less motional constraints lead to longer T_2, it is expected that $T_{2C} < T_{2I} < T_{2A}$. In this work, the ^{1}H-FID of a semi-crystalline polymer material is represented by a somewhat generalized, empirical equation:

$$I = I_C \frac{\sin(\Delta\omega t)}{\Delta\omega t} \mathrm{Exp}\left[-\left(\frac{t}{T_{2C}}\right)^{d_C}\right] + I_I \mathrm{Exp}\left[-\left(\frac{t}{T_{2I}}\right)^{d_I}\right] + I_A \mathrm{Exp}\left[-\left(\frac{t}{T_{A3}}\right)^{d_A}\right]. \tag{3}$$

The parameters d_C, d_I, and d_A represent the respective "shape factors" and will be commented on later in this section. The parameter $\Delta\omega$ characterizes the "beat-shape" of FID component C [the first term in Eq. (3)]. We note that as $\Delta\omega$ approaches zero (no beat shape), the factor $\frac{\sin(\Delta\omega t)}{\Delta\omega t}$ approaches 1, and the FID component C becomes—mathematically—equivalent to FID components I and A.

For simplicity, if no ambiguity appears, the big letter P will be used when referring to any of the ten adjustable parameters: I_C, I_I, I_A, T_{2C}, T_{2I}, T_{2A}, d_C, d_I, d_A and $\Delta\omega$ in Eq. (3). Likewise, the symbol $\overline{P}$ will be used to represent the average value of P. It is worth noting that many researchers keep the shape factors fixed, i.e., $d_C = 2$, $d_I = 1$ or 2, and $d_A = 1$. However, these assumptions may be questionable.

The non-crystalline domains (I and A) are likely to be both structurally and dynamically heterogeneous and therefore are best represented by some distribution of spin–spin relaxation times T_2. Hence, some authors add extra Gaussian and/or exponential terms to Eq. (3). This, however, introduces additional adjustable parameters, which may affect the robustness of the model, making it numerically less stable by introducing significant inter-dependence between the adjustable parameters.

It is reasonable to ask why the shape parameter d_C may take a value different from two (2). From basic theory, it follows that the (static) dipolar interaction term $\Delta\omega$ is proportional to the inverse cube of the distance r between nuclei. Hence, the following equation results for PE: $\frac{\Delta\omega}{2\pi}(\mathrm{kHz}) \approx 122 \frac{1}{r(\text{Å})^3}$. Since the distance between a methylene proton and its neighboring protons vary, it follows that the first term in Eq. (3)—the Abragamian—must be modified accordingly, i.e.:

$$I = I_C \sum_i f_i \frac{\sin\left(\frac{3}{2}\Delta\omega_i t\right)}{\left(\frac{3}{2}\Delta\omega_i t\right)} \mathrm{Exp}\left[-\left(\frac{t}{T_{2C,i}}\right)^2\right], \tag{4a}$$

where f_i represents the number-fraction of protons at the same distance from the reference proton (the factor 3/2 appears due to the spatial averaging of the dipolar interaction) as discussed by Räntzsch and coworkers [12]. Hence, Eq. (4a) can be identified as a distribution of Gaussian functions. In this respect, Hansen and coworkers [13] have shown that the distribution of Gaussian functions can be approximated by the function $Y = \mathrm{Exp}\left[-\left(\frac{t}{T_2}\right)^d\right]$ with $1 < d < 2$ and is denoted a "compressed exponential" or Weibullian function in which shape becomes more skewed and flattened as d decreases (from 2 to 1). Although this distribution is constraint, it has the advantage of being simple, numerically flexible, and to contain only one additional and adjustable parameter.

Likewise, the third term in Eq. (3) ($0 < d_A < 1$), which is denoted a "stretch exponential" function, can be interpreted as a distribution of exponential functions, which shape also broadens as d_A decreases (from 1 to 0) [13]. Anyhow, for both distributions, their average spin–spin relaxation time $\langle T_{2X} \rangle$ can be expressed by:

$$\langle T_{2X} \rangle = \frac{T_{2X}}{d_X} \Gamma\left(d_X\right), \tag{4b}$$

where $X = C, I \mathrm{or} A$ and Γ defines the Gamma function. T_{2X} is characteristics relaxation rate estimated by compressed or stretch relaxation functions [14].

Pake was the first to derive an analytical expression for the line shape of interacting spin-1/2 nuclei, which inverse Fourier transform represents the corresponding FID. However, this inverse transformation results in a rather complex function, which is difficult to handle numerically [15]. Later, however, Abragam [16] suggested a much simpler, phenomenological expression for this crystalline FID component, which is simply referred to as an "Abragamian" and is represented by the first term in Eq. (3). Despite its simplicity, it has been shown to give a good representation of the FID from other regular, crystalline lattices, as for instance semi-crystalline polyolefins.

Finally, we recognize that the initial signal intensity ($t = 0$) of all three FID components in Eq. (3) will have decreased by the same factor of (1/e) at time $t = T_2$. In the NMR community, however, it is more common to express the Gaussian function as $\mathrm{Exp}\left[-\frac{1}{2}\left(\frac{t}{T_2^*}\right)^2\right]$ rather than by $\mathrm{Exp}\left[-\left(\frac{t}{T_2}\right)^2\right]$ which implies that the T_2 reported in this work is systematically longer than the T_2^*, by a factor of $\sqrt{2}$.

4 Results and Discussion

4.1 Quantitative Sampling of FID

The results presented in this work rely on quantitative sampling of the FID, which is dictated by the longest spin–lattice relaxation time (T_1) within the sample. The T_1 is determined by applying a Saturation Recovery pulse sequence. The longitudinal relaxation curves of samples C, SC, and MC are shown in Fig. 1.

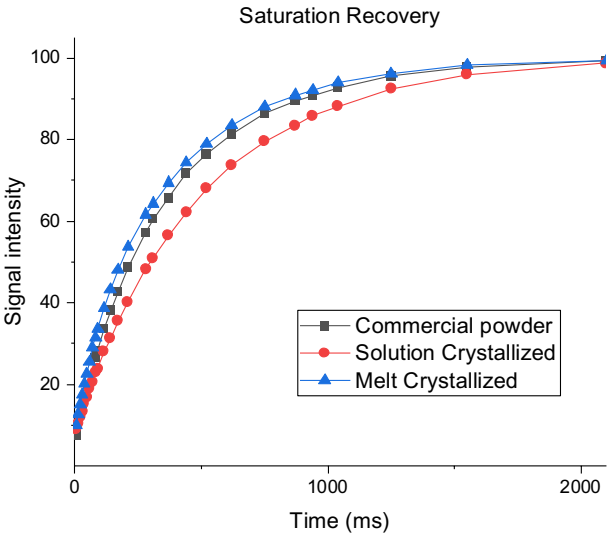

Fig. 1 Saturation recovery relaxation curves of samples C, SC, and MC were acquired at 60 °C. The solid curves represent exponential model fits, as discussed in the text

Two simple relaxation models: SEM (single exponential model) and DEM (double exponential model), were fitted to the observed relaxation curves in Fig. 1 (color dots) and their respective BIC number calculated, according to Eq. (2). In addition, a three-exponential relaxation model was also tested but resulted in no statistical improvement (no decrease in the BIC number) and was therefore excluded from any further analysis.

The best relaxation model was identified by the smaller BIC number (highlighted numbers in Table 1). The relaxation parameters are summarized in Table 2.

It is necessary to keep in mind that for a three-domain system (crystalline–intermediate–amorphous), three distinct T_1 times, each characterizing its particular

Table 1 BIC numbers were obtained by model-fitting two different relaxation models (SEM and DEM) to the observed relaxation curves of samples C, MC and SC (Fig. 1)

Model\samplel	C	SC	MC
SEM	408	**357**	428
DEM	**318**	386	**308**

Table 2 Relaxation parameters in samples S, SC, and MC, as derived from the best relaxation model (Table 1)

Parameter\model	C	SC	MC
I_1 (%)	78 ± 3	100.0 ± 0.2	79 ± 1
T_{11} (ms)	446 ± 9	495 ± 3	415 ± 5
I_2 (%)	22 ± 3		21 ± 1
T_{12} (ms)	149 ± 11		99 ± 4

domain, are expected. However, due to magnetization transfer between domains, as mediated by spin-diffusion, the number of detectable T_1 times may reduce to only a single T_1, as noticed for the SC sample. Generally, the number of distinct T_1 times will depend on the size of the domains and their spin-diffusion characteristics [17, 18]. Hence, the numerical values shown in Table 2 are mainly apparent and not representative of the true spin–lattice relaxation times and corresponding intensities of the domains. This topic is, however, outside the scope of this work. Therefore, we simply conclude from the data presented in Table 2 that the longitudinal magnetization will reach its equilibrium value within 4–5 times the longest $T_{1,}$ which—in this work—corresponds to a repetition time of the order of 2 s for all three samples.

4.2 Model Fitting of the FID

The model-fitting approach used throughout this work is exemplified by steps 1–3 below, with reference to the FID of sample MC shown in Fig. 2, and was acquired with NS = 256 scans, corresponding to a SNR_{FID} equal to 1590, as determined from Eq. (1). The fitting procedure is reviewed in steps 1–3:

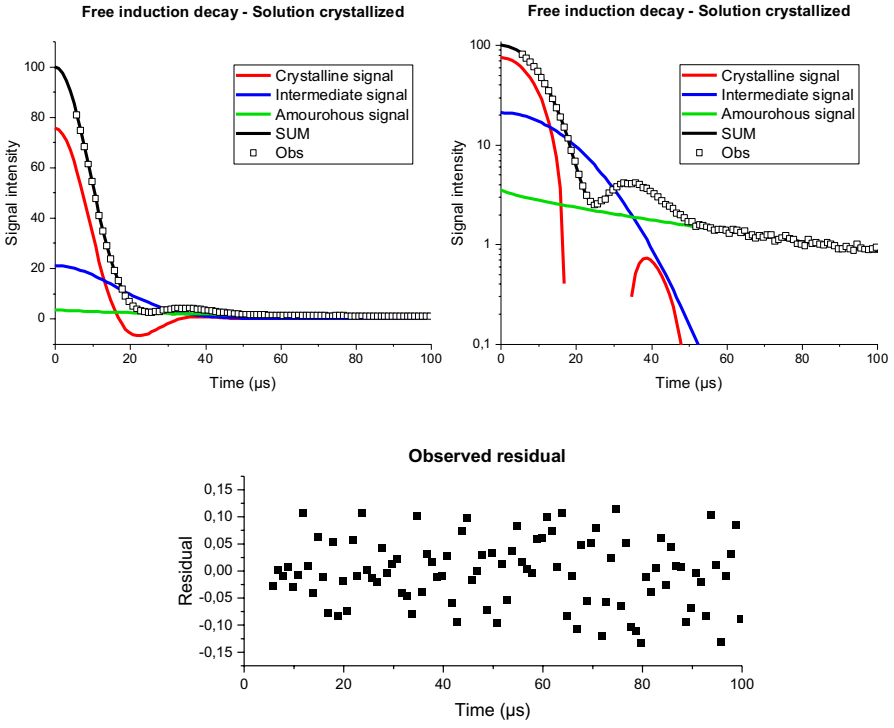

Fig. 2 Observed (square) and model-fitted (line) FID of sample MC (NS = 256) shown in a linear–linear plot (top left) and in a semi-logarithmic plot (top right). Three distinct FID components are identified and displayed by the red, blue, and green curves. (Bottom) Residual data, the difference between observed and model-fitted FIDs

1) Identify the longest spin–spin relaxation time component (A) in the FID by visual inspection (see Fig. 2 for $t \geq t_1 \approx 50$ µs) and fit the function $I_A \mathrm{Exp}\left[-\left(\frac{t}{T_{A3}}\right)^{d_A}\right]$ (for $t \geq t_1 = 50$ µs) to derive the parameters I_A, $T_{2A,}$ and d_A.
2) Determine the remaining seven (7) adjustable parameters by fitting Eq. (3) to the observed FID for all t by keeping I_A, $T_{2A,}$ and d_A (from step 1) fixed.
3) Perform a refinement by re-fitting Eq. (3) to the observed FID (for all t) using the parameters derived in steps 1–2 as initial input parameters.

All FIDs acquired in this work reveal three distinct components with relative intensities I_C:I_I:I_A as illustrated by the colored curves in Fig. 2.

Regarding the shape factor d_C in Eq. (3), Uehara et al. suggested that this parameter may differ from two in UHMWPE samples and exemplified this in Ref. [19]. However, no explicit numerical value of d_C was presented. This important issue was pursued in this work by comparing the BIC numbers derived by fitting two different models to the same observed FID. The two models differed only by the constraint put on the parameter d_C. i.e., d_C was freely adjustable (model I), and d_C was constant and equal to two (model II). The results from the above BIC analysis are summarized in Table 3 and show that the FID model represented by Eq. (5) is the better model. Hence, Eq. (3) was replaced by Eq. (5) in the rest of this work.

$$I = I_C \frac{\sin(\Delta\omega t)}{\Delta\omega t} \mathrm{Exp}\left[-\left(\frac{t}{T_{2C}}\right)^2\right] + I_I \mathrm{Exp}\left[-\left(\frac{t}{T_{2I}}\right)^{d_I}\right] + I_A \mathrm{Exp}\left[-\left(\frac{t}{T_{A3}}\right)^{d_A}\right]. \tag{5}$$

4.3 Standard Error $\sigma(P)$ in P as Derived by the Model Fitting of FID

The typical beat shape of the crystalline FID component of sample MC is clearly recognized from its intersection with the time axis at $t_p \approx 16.8$ µs, ≈ 33.3 µs, and 50.0 µs in Fig. 2 (top). Additional intersection points at longer times are not

Table 3 Difference (ΔBIC) between the BIC numbers (ΔBIC) derived from two different FID models that were fitted to the same observed FIDs of samples C, MC, and SC, respectively

NS\sample	ΔBIC = BIC (Model I) − BIC(Model II)		
	MC	SC	C
256	7	8	
512	12	7	
1024	13	6	
2048	7	8	3
3072	7	7	7
4096	6	7	6

The two FID models differed only by (a) d_C being freely adjustable in Eq. (3) (Model I) and (b) d_C being fixed and equal to two in Eq. (3) (Model II)

NS number of scans

detectable as the FID signal disappears in the noise. According to Eq. (5), the intersection points will appear at time t_p satisfying the equation; $\sin\left(\Delta\omega \cdot t_p\right) = n \cdot \pi$ with $n = 1, 2, 3,\ldots$ and correspond well with $\Delta\omega = (1.893 \pm 0.005)\text{s}^{-1}$, as derived by model-fitting (Table 4).

Furthermore, the two remaining FID components (I and A) are identified by the dotted/dashed curves in the same figure. In particular, the small and random distribution of residuals between observed- and model-fitted FID demonstrates the good quality of the model.

Similar high-quality model fits were obtained on all observed FIDs of sample MC. The derived parameters (P) and corresponding standard deviations $\sigma(P)$ versus SNR_{FID} are summarized in Table 4. Not surprisingly, $\sigma(P)$ is found to decrease with increasing SNR_{FID}. To understand these results more quantitatively, it is necessary to expand the experimental work to include reproducibility measurements and to obtain FIDs with additional and higher SNR_{FID}.

Unfortunately, since such an extended experimental work may become rather time-consuming, we decided to choose an alternative strategy; to generate synthetic FIDs by Monte Carlo simulations, i.e., to synthesize FIDs with predefined parameters (P) and predefined noise, followed by model fitting. This approach was found to be both profitable and advantageous and is reviewed in the next section.

4.4 Synthetic FIDs (Monte Carlo Simulations)

To generate synthetic FIDs, the following protocol was applied:

1) Insert a suitable and relevant set of parameters P in Eq. (5).
2) "Normalize" the FID ($I_C + I_I + I_A = I_0 = 100$ at time $t = 0$).
3) Generate a synthetic FID by adding a preset, random noise term SNR_{FID} [see Eq. (1)] to Eq. (5).

Table 4 Parameter P and corresponding standard error $\sigma(P)$ as obtained by model fitting Eq. (5) to the observed FID of samples SC, commercial, and MC, acquired with NS = 4096

Parameter\sample	SC	Commercial	MC
SNR_{FID} (NS)	4117 (4096)	5950 (4096)	4212 (4096)
I_C (%)	74.3 (1.6)	62.6 (1.0)	43.1 (0.21)
$\Delta\omega$ (μs^{-1})	0.1868 (0.0010)	0.1817 (0.0006)	0.1887 (0.0002)
T_{2C} (μs)	25.0 (0.21)	23.6 (0.32)	24.7 (0.10)
I_I (%)	23 (1.7)	30.4 (1.3)	29.6 (1.2)
d_I	1.97 (0.08)	1.92 (0.05)	1.03 (0.02)
T_{2I} (μs)	22.1 (0.9)	24.3 (0.47)	28.5 (0.25)
I_A (%)	3.2 (0.15)	7.1 (0.6)	27.2 (0.97)
d_A	0.82 (0.02)	1.32 (0.05)	0.99 (0.012)
T_{2A} (μs)	69 (3.6)	47.3 (2.6)	89 (2.2)

The number in parenthesis is $\sigma(P)$

4) Fit Eq. (5) to the synthetic FID to derive P and their corresponding standard error $\sigma(P)$.
5) Repeat steps 3 and 4 a number of times N (validate the reproducibility).
6) Calculate the average $\overline{\sigma(P)}$ of $\sigma(P)$ and its dispersion or standard deviation $\sigma\left(\overline{\sigma(P)}\right)$ from the data obtained in steps 4, 5.
7) Repeat steps 3–6 for the new $\mathrm{SNR}_{\mathrm{FID}}$.

4.5 Error Bound $\sigma^{+}(P)$ of the Standard Error $\sigma(P)$ as Derived from a Synthetic FID Analysis

An application of the protocol presented in Sect. 4.4 is illustrated in Fig. 3 where 12 synthetic FIDs were generated from Eq. (5) by inserting the parameters P from the last column of Table 4 (sample MC) with $\mathrm{SNR}_{\mathrm{FID}}$ fixed to 1600. This initial step was followed by fitting Eq. (5) to each synthetic FID to derive the parameters P and their corresponding standard error $\sigma(P)$. For simplicity, only the results of the parameter $P = T_{2I}$ (filled square) is shown in Fig. 3, from which the following parameters were calculated:

$$\overline{P} = \frac{1}{N}\sum_{i=1}^{N} P_i, \tag{6a}$$

$$\overline{\sigma(P)} = \frac{1}{N}\sum_{i=1}^{N} \sigma(P)_i, \tag{6b}$$

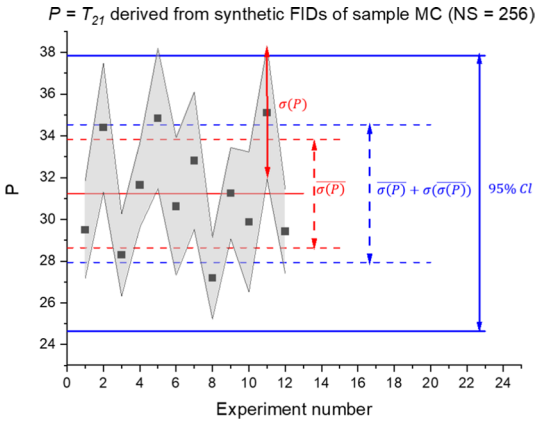

Fig. 3 $P = T_{2I}$ (filled square) of 12 synthetically generated FIDs, according to the procedure presented in Sect. 4.4. All symbols are defined in the text where the average $(\overline{T_{2I}})$ is represented by the horizontal (red) line, the standard error $\sigma\left(T_{2I}\right)$ is illustrated by the vertical, solid (red) line, and the average standard error $\sigma(T_{2I})$ is illustrated by the vertical, dotted (red) arrow. Finally, the upper confidence bound—as defined by Eq. (7a)—is plotted for $t = 1$ (dotted, blue, arrow) and for $t = 2.5$ (solid, blue, arrow) in which the latter corresponds to a 95% confidence limit (CL)

$$\sigma\left(\overline{\sigma(P)}\right) = \sqrt{\frac{\left(\sigma(P)_i - \overline{\sigma(P)}\right)^2}{N-1}}, \tag{6c}$$

where $\sigma\left(\overline{\sigma(P)}\right)$ represents the dispersion or spread in $\overline{\sigma(P)}$. Hence, we define an upper bound $\sigma^+(P)$ of $\sigma(P)$ according to Eq. (7a):

$$\sigma^+(P) = \overline{\sigma(P)} + t \cdot \sigma\left(\overline{\sigma(P)}\right), \tag{7a}$$

where t is a factor defining the size of the confidence interval of P which is normally set to $t=2$ (90% confidence interval), $t=2.5$ (95% confidence interval) or $t=3$ (99% confidence interval). In this work, we use $t=2.5$.

Additional synthetic FIDs were generated using the same P values but different $\mathrm{SNR_{FID}}$, ranging from 500 to 16,000. The above procedure was repeated after replacing the P values of sample MC with the corresponding P values of samples SC and commercial (Table 4), respectively.

A critical evaluation of all derived data (using Eqs. 6b and 6c) revealed that both $\overline{\sigma(P)}$ and $\sigma\left(\overline{\sigma(P)}\right)$ could be excellently represented by a power-law relation with respect to $\mathrm{SNR_{FID}}$, i.e.:

$$\overline{\sigma(P)} = \alpha(P) \cdot \left[\mathrm{SNR_{FID}}\right]^{-q_0}, \tag{7b}$$

with $q_0 = 1.00 \pm 0.04$ and:

$$\sigma\left(\overline{\sigma(P)}\right) = \beta(P) \cdot \left[\mathrm{SNR_{FID}}\right]^{-q_1}, \tag{7c}$$

with $q_1(\mathrm{commercial}) \approx q_1(\mathrm{SC}) = 1.34 \pm 0.06$ and $q(\mathrm{MC}) = 1.73 \pm 0.06$ and $\alpha(P)$ and $\beta(P)$ being constants, for fixed P and q.Hence, the generalized expression for the upper (95%) error bound of $\sigma(P)$ reads:

$$\sigma^+(P) = \alpha(P)\frac{1}{\left[\mathrm{SNR_{FID}}\right]} + \beta(P)\frac{1}{\left[\mathrm{SNR_{FID}}\right]^{q_1}}. \tag{8}$$

The significance of the second term in Eq. (8) is illustrated in Fig. 4, which shows a plot of the relative upper bound $\sigma\left(\overline{\sigma_R(P)}\right)/\overline{\sigma_R(P)}$ versus $\overline{\sigma_R(P)} = \overline{\sigma(P)}/\overline{P}$ and suggests that the largest contribution from the dispersion term $\sigma\left(\overline{\sigma_R(P)}\right)$ appears when $\mathrm{SNR_{FID}}$ is low and/or when at least one of the components C, I or A are small. In about 65% of the data shown in Fig. 4, the term $\sigma\left(\overline{\sigma_R(P)}\right)$ contributes with less than 10% to $\sigma^+(P)$ and about 35% contribute with between 10 and 25%. Hence, only a minor fraction ($\approx$ 10%) contributes by more than 25%.

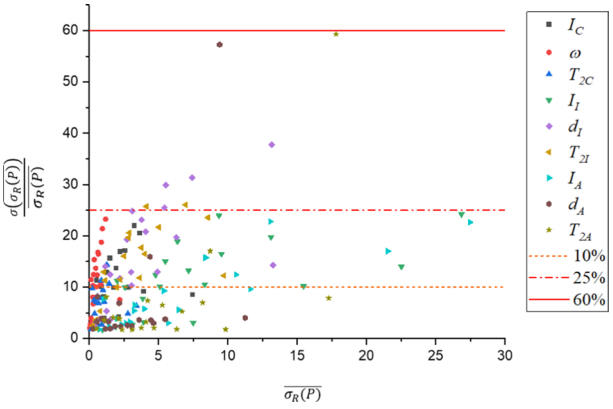

Fig. 4 The relative dispersion $\frac{\sigma\left(\overline{\sigma_R(P)}\right)}{\overline{\sigma_R(P)}}$ versus $\overline{\sigma_R(P)}$ for all P, as obtained from the synthetic FIDs of samples C, SC, and MC (> 180 synthetic FIDs). The dashed lines represent different levels (10%, 25%, and 60%) of contribution from the term $\sigma\left(\overline{\sigma_R(P)}\right)$. The numbers 1–9 refer to the nine adjustable parameters P in Eq. (5)

4.6 Standard Error $\sigma(P)$ Versus SNR_{FID}: Experimental Results

The upper (95% confidence) relative error bounds $\sigma_R^+(P)$, as derived from the synthetic FID analysis discussed in the previous section, are plotted against SNR_{FID} in Figs. 5, 6 and 7 for all parameters P of the UHMWPE samples MC, SC, and C (commercial), respectively.

As expected, all observed relative errors $\sigma_R(P)$ are smaller or equal to $\sigma_R^+(P)$, except for the parameter $P = I_A$ of sample MC (Fig. 5), which is found to be slightly above $\sigma_R^+(I_A)$. This is surprising when keeping in mind that the MC sample has the highest amorphous fraction (I_A) of the three samples. Hence, we believe this discrepancy to be accidental and that I_A represents an outlier (1 out of 142 data points).

Recalling that the external magnetic field is characterized by a time constant T_2^* of the order of 150 µs (see Sect. 2.2) and that the spin–spin relaxation time T_{2A} is approximately 90 µs, both the derived shape factor (d_A) and the spin–spin relaxation time (T_{2A}) are expected to be affected by these magnetic field heterogeneities. Likewise, since the observed T_{2A} within the two other samples are of the order of 45 µs (commercial sample) and 69 µs (SC sample), they are probably affected by magnetic field heterogeneities, as well, although to a lesser extent. Actually, this conclusion is supported by CPMG experiments (not shown), which revealed a significantly longer T_{2A} as compared to the same parameter derived from the FID. Hence, we will not go into any further discussion regarding the data of the amorphous phase A (Fig. 5). Figure 5 is mainly included for the sake of completeness.

Before discussing the results displayed in Figs. 6 and 7 in more detail, it is of more practical interest to see how the relative standard error of the derived parameters P depends on the sampling time ($T_{sampling}$), i.e., the overall time to acquire the FID. Since the maximum spin–lattice relaxation time $T_{1,\,max}$ was less than

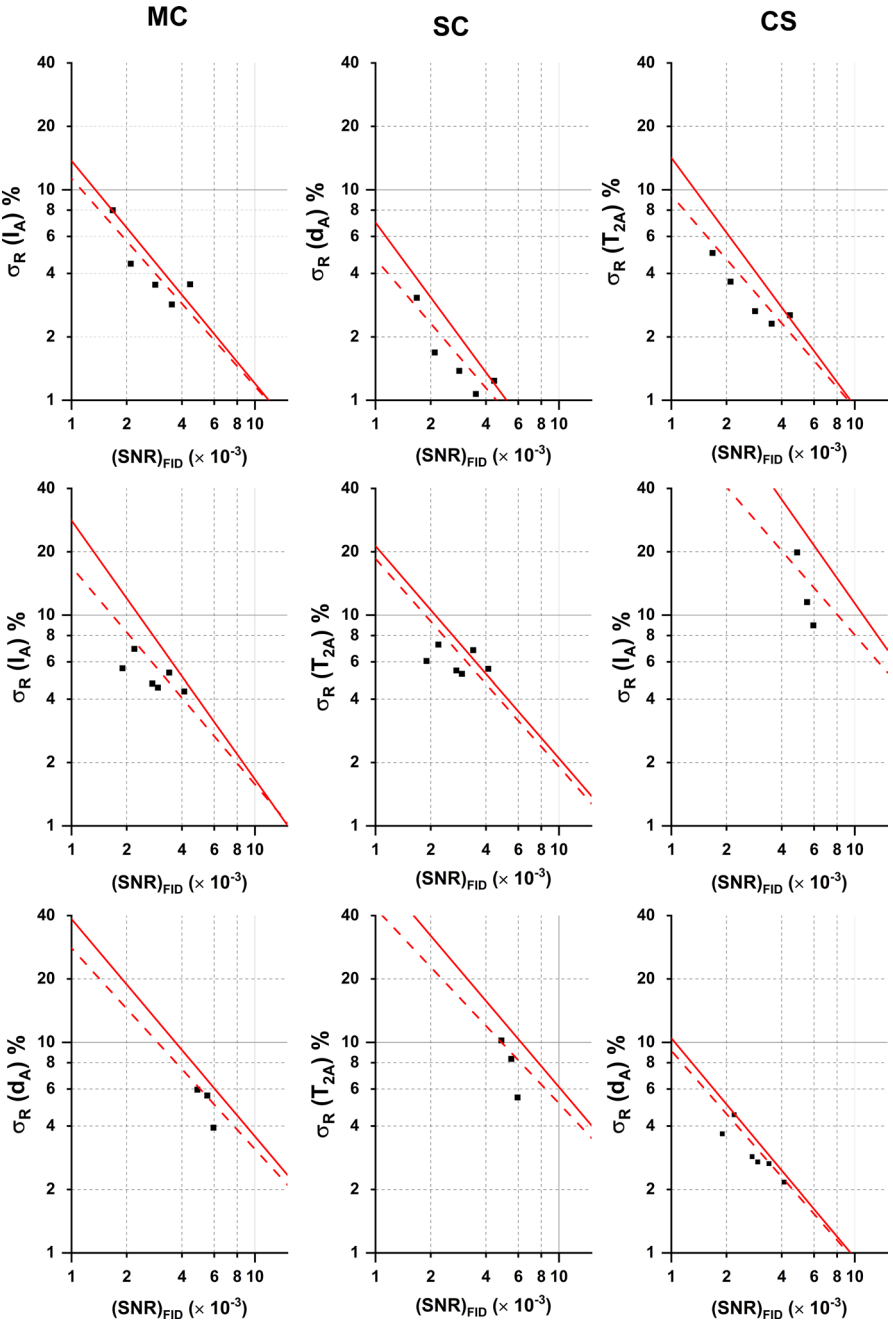

Fig. 5 Relative standard deviation $s_R(P)$ (dashed line) and corresponding upper 95% confidence limit $\sigma_R^+(P)$ (line) of NMR parameters P (=I_A, T_{2A}, and d_A) [see Eq. (5)] within the amorphous domain (A) as a function of the signal-to noise ratio (SNR_{FID}) of the FID of samples MC, SC, and C, as derived by Monte Carlo simulation. The black dots represent experimental data

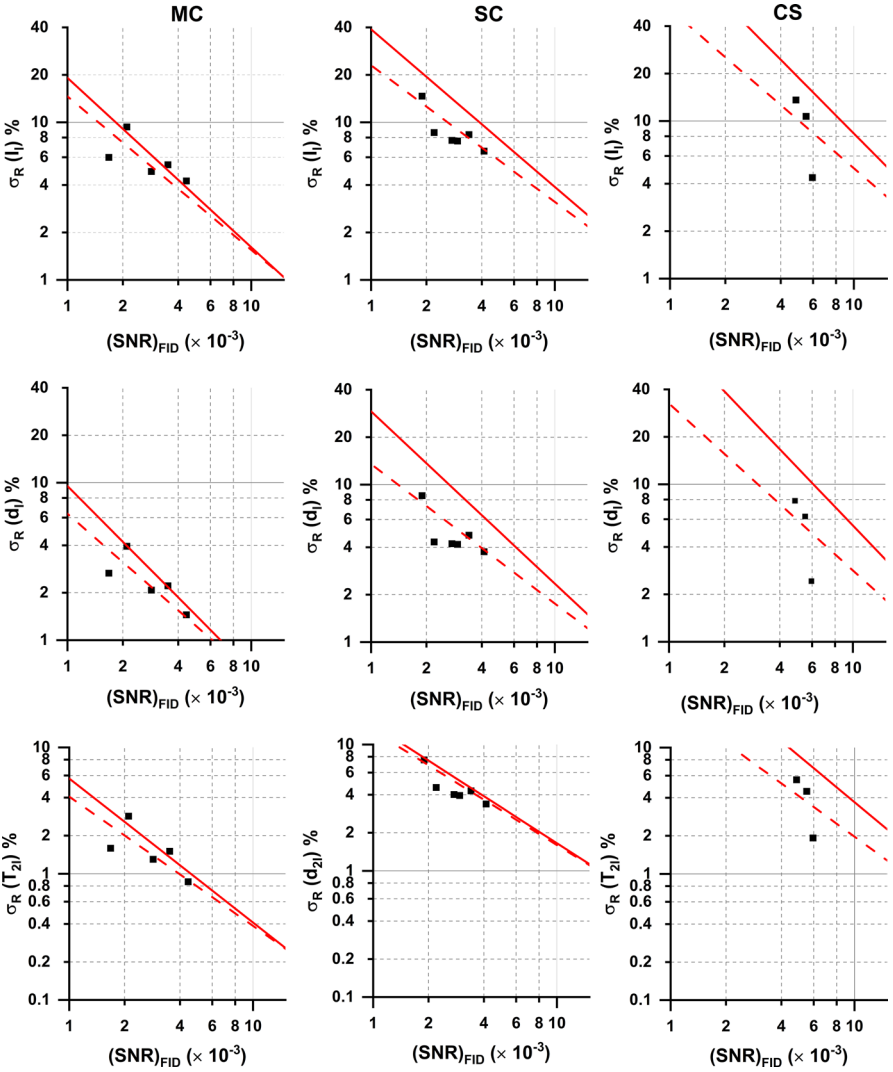

Fig. 6 Relative standard deviation $s_R(P)$ (dashed line) and corresponding upper 95% confidence limit $\sigma_R^+(P)$ (line) of NMR parameters P ($=I_I$, T_{2I}, and d_I) within the intermediate domain (I) as a function of the signal-to-noise ratio (SNR_{FID}) of the FID of samples MC, SC, and C as derived by Monte Carlo simulation. The black dots represent experimental data

0.5 s and the repetition time between scans must be set to 4–5 times longer than the maximum spin–lattice relaxation time to obtain quantitative data, it follows that: $T_{\text{sampling}} \sim 5 \cdot T_{1\,\text{max}} \cdot \text{NS}$. Since the calibration experiments revealed that $\text{SNR}_{\text{FID}} = (57 \pm 2)\sqrt{\text{NS}}$, we obtain:

$$T_{\text{sampling}} \approx (7.7 \pm 0.5) \cdot 10^{-4} \cdot \text{SNR}_{\text{FID}}^2. \tag{9}$$

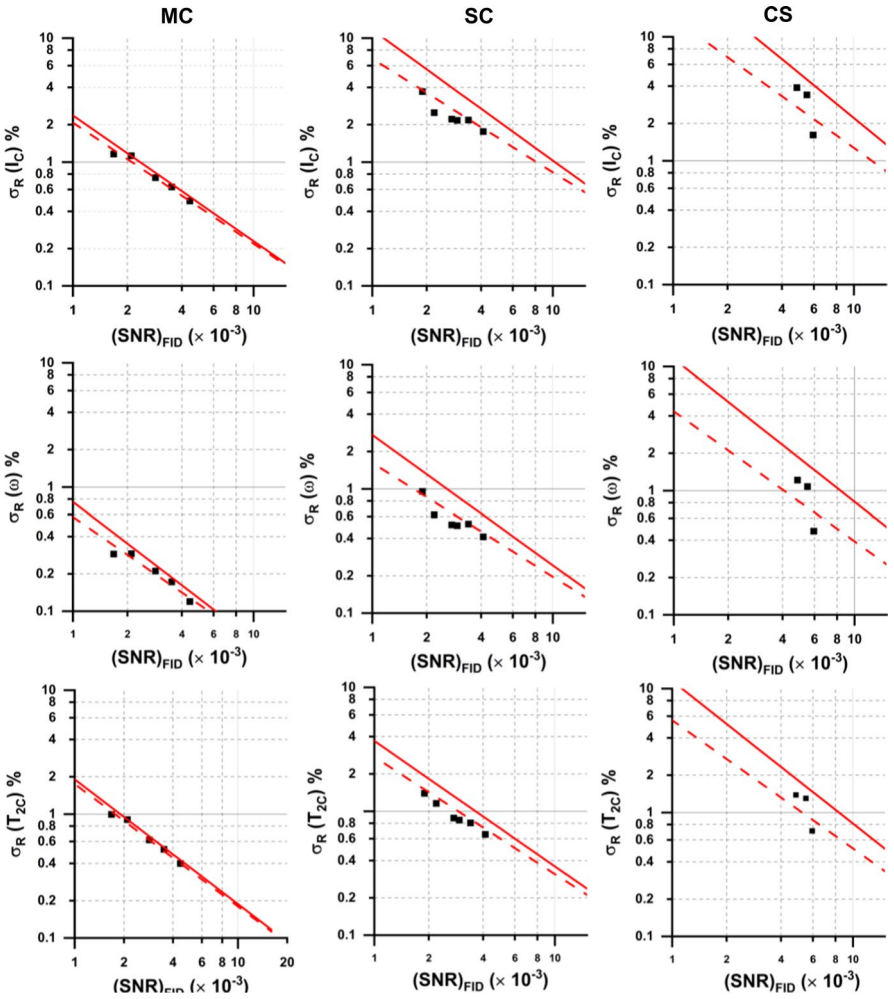

Fig. 7 Relative standard deviation $s_R(P)$ (dashed line) and corresponding upper 95% confidence limit $\sigma_R^+(P)$ (line) of NMR parameters P ($=I_C$, T_{2C} and ω) within the crystalline domain (C) as a function of the signal-to-noise ratio (SNR_{FID}) of the FID of samples MC, SC, and C as derived by Monte Carlo simulation. The black dots represent experimental data

Hence, by combining Eqs. (8) and (9), the minimum sampling time necessary to obtain a preset relative standard error of any parameter P can be determined. The results are summarized in Table 5. and show that an upper relative error in P of about 5% can be obtained for all P within about 5 h sampling time. To reach a level of 1% in the upper relative error of P takes more than 12 h (except for $P = T_{2C}$ and ω) and may be rather demanding due to—for instance—instability in the magnetic field. We checked this potential source of error by sampling an FID for 1 h and storing the data before a second FID was acquired after optimizing

Table 5 The minimum sampling time ($T_{sampling}$) required to obtain a preset "upper relative error bound" $\sigma_R^+(P)$ within the range of 0.1–7.5% (95% confidence interval) of the parameter $P = I_C$, T_{2C}, ω, I_I, T_{2I}, and d_I as obtained by model-fitting Eq. (5) to the observed FIDs of samples MC, SC, and C

P	$\sigma_R^+(P)$/%	$T_{sampling}$(*)		
		MC	SC	C
I_C	7.5	57 (s)	656 (s)	0.736 (h)
	5	130 (s)	0.446 (h)	1.61 (h)
	2.5	534 (s)	2.07 (h)	6.09 (h)
	1	0.97 (h)	15.6 (h)	35.3 (h)
T_{2C}	7.5	40 (s)	91 (s)	428 (s)
	5	92 (s)	211 (s)	935 (s)
	2.5	374 (s)	0.252 (h)	0.989 (h)
	1	0.655 (h)	1.73 (h)	5.67 (h)
ω	2.5	41 (s)	298 (s)	0.617 (h)
	1	254 (s)	0.604 (h)	3.54 (h)
	0.5	1002 (s)	2.73 (h)	13.2 (h)
	0.25	1.11 (h)	12.4 (h)	49.7 (h)
I_I	7.5	0.841 (h)	2.13 (h)	0.425 (h)
	5	1.93 (h)	5.22 (h)	1.61 (h)
	2.5	8.00 (h)	24.1 (h)	6.09 (h)
	1	52.0 (h)	182 (h)	34.8 (h)
d_I	7.5	588 (s)	0.894 (h)	3.54 (h)
	5	0.359 (h)	2.27 (h)	7.65 (h)
	2.5	1.37 (h)	11.3 (h)	28.75 (h)
	1	8.12 (h)	93 (h)	162 (h)
$^{**}T_{2I}$	7.5	25 (s)	0.78 (h)	1.76 (h)
	5	461 (s)	1.95 (h)	3.79 (h)
	2.5	0.583 (h)	9.37 (h)	14.1 (h)
	1	3.41 (h)	74 (h)	79.9 (h)

(*) s; seconds and h; hours

the on-resonance condition. This same procedure was repeated five (5) times, and the five FIDs were subsequently added together, and the SNR was determined. Finally, an FID of the same sample was acquired for 5 h, followed by an SNR measurement. Fortunately, no statistical difference between the two SNRs was found, at least for a sampling time of 5 h.

When model fitting a synthetic FID by a non-linear-least-squares (NLLS) procedure, the error in the derived parameters was frequently noticed to be significantly smaller than the "average" error determined from a series of identical FIDs with the same SNR_{FID}.

For example, a significant difference between PA and PB often appears when comparing the parameter P and its corresponding error $\sigma(P)$, as derived by model fitting the FID of two identical samples A and B. This difference is "apparent" in the sense that it originates from "poor" reproducibility. Notably, this effect is observed more frequently in FIDs of low SNR_{FID} and FID components of low relative intensity.

4.7 FID Simulation (A)

Within the context of this work, the word "different" refers to whether a measured NMR parameter (T_2, d, I and ω) of two samples A and B are different. Notably, this requires that the confidence interval of the measured parameter P is defined. The most frequently used confidence intervals in statistical applications are 90%, 95%, or 99%, respectively.

It is known that low-field NMR is hampered by a relatively poor signal-to-noise ratio, and that the sampling time for acquiring a "good" FID may be rather long. Hence, is it possible to predict the minimum number of scans (or equivalently, a minimum sampling time) to be acquired in the NMR experiment to ensure that the same two parameters P, as derived from two samples A and B, are statistically different? This question will be elaborated in this section with reference to Monte Carlo simulations performed on samples MC and SC (Figs. 8, 9) and will be restricted to the parameters $P = T_{2C}$, I_C and ω of domain C and the parameters $P = T_{2I}$, I_I and d_I of domain I. A corresponding analysis of the parameters in domain A is possible. Still, it is of less practical importance, as this FID component is systematically biased for acquisition times longer than 150 µs due to magnetic field inhomogeneity (see Sect. 2.2). Nevertheless, the advantage and benefits of applying Monte Carlo simulations will be outlined.

The parameters derived by fitting Eq. (5) to the observed FIDs of samples MC and SC are shown in Table 6 for $\mathrm{SNR_{FID}} \approx 4000$ and were used as input values in the subsequent Monte Carlo simulations to estimate the 95% confidence interval (Eq. 7a) of each parameter P as a function of $\mathrm{SNR_{FID}}$. The results are illustrated in Fig. 8, showing the upper (s^+) and the lower (s^-) 95% confidence limits of parameter P in samples MC (blue) and sample SC (red).

For example, no overlap between the 95% confidence intervals of I_C in samples MC (blue) and SC (red) is recognized for $\mathrm{SNR_{FID}} > 200$. Hence, I_C of samples MC and SC are significantly different (within a 95% confidence interval), even for a relatively small $\mathrm{SNR_{FID}}$, of the order of 200.

In contrast, the corresponding 95% confidence interval of parameters I_I, T_{2I}, and d_I (domain I) of samples MC and SC (Fig. 8a, c, e) reveals significant overlaps. Hence, a "critical" value of $\mathrm{SNR_{FID}}$ is introduced, which as defined by the smallest value of $\mathrm{SNR_{FID}}$ at which the two confidence intervals no longer overlap. This critical value appears at the intersection between the lower 95% confidence limit (s^-) of one sample and the higher 95% confidence limit (s^+) of the other sample, as illustrated by the vertical (black) line in the respective figures, and corresponds to $\mathrm{SNR_{FID}} = 725$ (d_I), 900 (T_{2I}) and 1900 (I_I), respectively. Since the repetition time t_p (= 2 s) between scans is known and $\mathrm{SNR_{FID}}$ is proportional to $\sqrt{\mathrm{NS}}$ ($= (0.0175 \pm 0.0005) \cdot \mathrm{SNR_{FID}}$), the time at which the critical $\mathrm{SNR_{FID}}$ is reached corresponds to 1.2 min (T_{2I}), 2.5 min (d_I), and 21 min (I_I), respectively.

The final two parameters, T_{2C} (Fig. 8d) and ω (Fig. 8f) of the C-domain reveal an intersection between their respective confidence limits at a much higher $\mathrm{SNR_{FID}}$, of about 6000 and 4000 and correspond to a time at which the critical $\mathrm{SNR_{FID}}$ is achieved at 1.7 h (ω) and 4.1 h (T_{2C}), respectively.

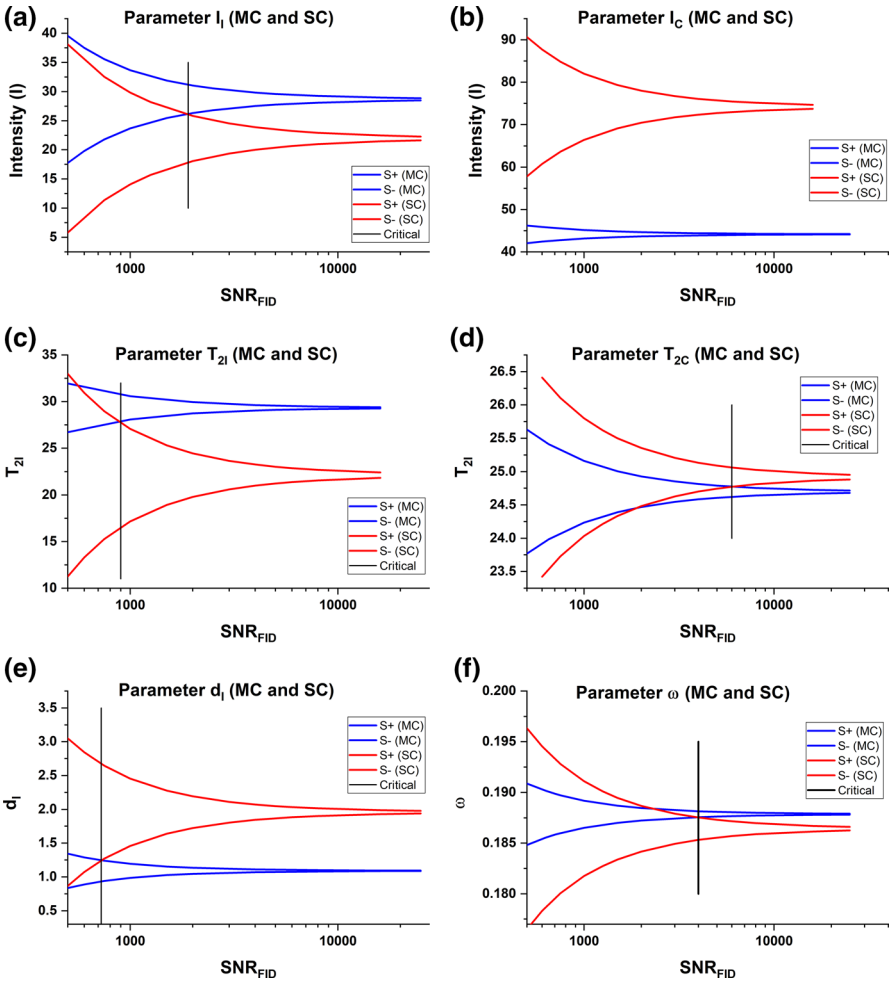

Fig. 8 95% confidence interval limits (s^+ and s^-) of parameter $P = T_{2C}$, I_C and ω (domain C) and $P = T_{2I}$, I_I and d_I (domain I) for samples MC and SC as a function of SNR_{FID}, as derived from Monte Carlo simulations. The vertical, solid line (black) represents the "critical" SNR_{FID}. See text for further details

Hence, the minimum sampling time necessary to decide whether the (same) model-derived parameters within two different samples are statistically different (95% confidence interval) can be estimated and preset, before initiating an actual experiment.

4.8 FID Simulations (II)

In the discussion presented in the previous section, it was implicitly assumed that the average value $\overline{P}$ of any parameter, P was error-free, which is obviously a rough assumption. An error $\sigma(\overline{P})$ in $\overline{P}$ will affect the estimate of the critical

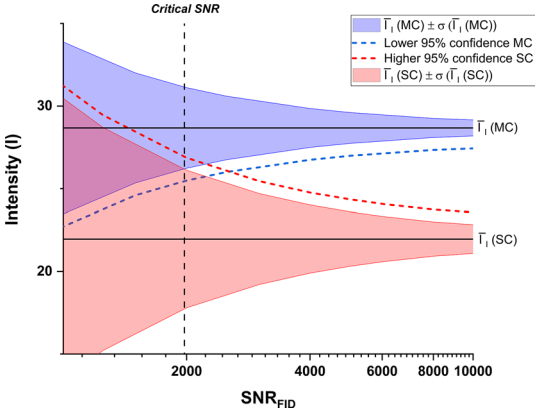

Fig. 9 95% confidence intervals of the model-derived parameter $P = I_I$ as a function of $\mathrm{SNR}_{\mathrm{FID}}$ for samples MC (red) and SC (blue). The solid horizontal line (black) represents the average value $\overline{I_I}$(MC) and $\overline{I_I}$(SC), the shaded area corresponds to the error windows of $\pm\sigma\left(\overline{I_I}(\mathrm{MC})\right)$ and $\pm\sigma\left(\overline{I_I}(\mathrm{SC})\right)$ of $\overline{I_I}$(MC) and $\overline{I_I}$(SC), respectively. The shift in the lower (red) and upper (red) 95% confidence limits of $\overline{I_I}$(MC) and $\overline{I_I}$(SC), is illustrated by dashed lines with corresponding colors. The relative value of $\sigma\left(\overline{I_I}(\mathrm{MC})\right)$ and $\sigma\left(\overline{I_I}(\mathrm{SC})\right)$ was set 3% and 5%, respectively. See text for further details

Table 6 NMR parameters derived by NLLSQ-fits of Eq. (5) to the observed FIDs of samples MC and SC with NS = 4096, respectively

P\sample	Solution crystallized		Melt crystallized	
	$\overline{P}(\sigma)$	CI	$\overline{P}(\sigma)$	CI
I_C (%)	74.3 (1.6)	71.1–77.5	43.1 (0.21)	42.7–43.5
ω (μs^{-1})	0.1868 (0.0010)	0.185–0.189	0.1887 (0.0002)	0.188–0.189
T_{2C} (μs)[a]	25.0 (0.2)	24.5–25.4	24.7 (0.10)	24.6–25.0
I_I (%)	23 (1.7)	19.1–25.9	29.6 (1.2)	28.4–33.5
d_I	1.97 (0.08)	1.80–2.00	1.03 (0.015)	0.99–1.05
T_{2I} (μs)	22.1 (0.9)	20.3–23.8	28.5 (0.25)	28.2–29.1
I_A (%)	3.2 (0.15)	2.9–3.5	27.2 (0.97)	24.0–27.9
d_A	0.82 (0.02)	0.77–0.86	0.99 (0.012)	0.99–1.04
T_{2A} (μs)	69 (3.6)	61.8–76.3	89 (2.2)	86.7–96.3

The standard error (σ) in P is shown in parentheses in which CI represents a 95% confidence interval

[a]According to the general definition of T_{2C} used within the NMR community, this relaxation time would be reported as $T_{2C}/\sqrt{2}$ ($\approx$ 17 μs)

value of $\mathrm{SNR}_{\mathrm{FID}}$ and will be discussed next. Figure 9 is a copy of Fig. 8a with the following additions: $\overline{I_I}$(MC) and $\overline{I_I}$(SC) represent the average value of I_I in samples MC and SC, as illustrated by the horizontal (black) line of sample MC. The shaded areas represent the respective error margins $\pm\sigma(\overline{I_I}(\mathrm{MC}))$ and $+\sigma(\overline{I_I}(\mathrm{SC}))$ of the same two samples. Consequently, the lower limit (s^-) of the 95% confidence interval of sample MC must be shifted vertically by the amount $\pm\sigma(\overline{P}(\mathrm{MC}))$ as illustrated by the solid/dashed curves (blue) in Fig. 9. Likewise, the upper limit

(s^+) of the 95% confidence interval in sample SC is shifted vertically by a corresponding amount $\pm\sigma(\overline{P}(\mathrm{SC})$, as illustrated by the solid/dashed curves (blue). According to the discussion presented in the previous section, the critical $\mathrm{SNR_{FID}}$ is located within the two vertical black lines, corresponding to an overall acquisition time of between 14 and 34 min, respectively. Hence, a minimum acquisition time of 34 min is acquired to attain a significant difference in $P = I_I$ between n the two samples.

5 Summary/Conclusion

A large number of experimental FIDs of three different UHMWPE samples were quired with different number of scans (NS) or transients to systematically vary the overall SNR of the FIDs ($\mathrm{SNR_{FID}}$). For each $\mathrm{SNR_{FID}}$, the corresponding FID was fitted to a generalized relaxation time model:

$$I = I_C \frac{\sin(\Delta\omega t)}{\Delta\omega t}\mathrm{Exp}\left[-\left(\frac{t}{T_{2C}}\right)^2\right] + I_I\mathrm{Exp}\left[-\left(\frac{t}{T_{2I}}\right)^{d_I}\right] + I_A\mathrm{Exp}\left[-\left(\frac{t}{T_{A3}}\right)^{d_A}\right].$$

in which the frequency factor $\Delta\omega$, the phase distributions (I_C, I_I, I_A), the spin–spin relaxation times (T_{2C}, T_{2I}, and T_{2A}), and shape factors (d_I, d_A). To simplify the discussion, we will use the notation P of any of these parameters. Due to the small, relative fraction of the amorphous phase in these polymer samples, we focus on the two non-amorphous domains C and I.

Finally, Monte Carlo simulations have been performed for each set of experimentally derived P values (for a given $\mathrm{SNR_{FID}}$) to generate synthetic FIDs. The upper and lower confidence limits $s^{\pm}(P)$ of P were determined and excellently represented by the following generalized equation (Eq. (8) in the text), i.e.;

$$s^{\pm}(P) = k(P)\cdot\left[\mathrm{SNR_{FID}}\right]^{-1} \pm t\cdot k'(P)\cdot\left[\mathrm{SNR_{FID}}\right]^{q},$$

where $k(P)$, $k'(P)$ and q ($1 < q < 2$) are constants, only dependent on the parameter P and the actual polymer system investigated. The parameter "t" defines the scaling factor of the confidence interval and equals 2.5 for a 95% confidence interval. The above equation is an empirical equation in which the first term represents the "average" of all model-derived deviations (on identical samples), and the second term represents the average spread of the same deviations.

An interesting spin-off from the above equation is that the minimum sampling time required to ensure a significant difference in the parameters $\mathrm{P_A}$ and $\mathrm{P_B}$ of two different samples A and B (within a specified confidence interval) can be calculated, and hence pre-set before initiating the experiment.

Acknowledgements The authors acknowledge the Research Council of Norway (RCN) for the financial support of the present work (project grant no 295595). We would like to specially thank Dr. Siw Bodil Fredriksen and Dr. Sara Ronasi from Norner Research AS for their never-ending support.

Funding Open access funding provided by University of Oslo (incl Oslo University Hospital).

References

1. P. Smith, P. Lemstra, J. Pijpers, A. Kiel, Ultra-drawing of high molecular weight polyethylene cast from solution. Colloid Polym. Sci. **259**(11), 1070–1080 (1981)
2. R. Schaller, K. Feldman, P. Smith, T.A. Tervoort, High-performance polyethylene fibers "al dente": improved gel-spinning of ultrahigh molecular weight polyethylene using vegetable oils. Macromolecules **48**(24), 8877–8884 (2015)
3. R. Bärenwald et al., Local flips and chain motion in polyethylene crystallites: a comparison of melt-crystallized samples, reactor powders, and nanocrystals. Macromolecules **47**(15), 5163–5173 (2014)
4. V. Litvinov, Molecular mobility and phase composition in polyolefins: from fundamental to applied research, in *NMR spectroscopy of polymers: innovative strategies for complex macromolecules*. (ACS Publications, Washington, 2011), pp. 179–190
5. S. Rastogi, D.R. Lippits, A.E. Terry, P.J. Lemstra, The role of the interphase on the chain mobility and melting of semi-crystalline polymers; a study on polyethylenes, in *Progress in understanding of polymer crystallization*. (Springer, Berlin, 2007), pp. 285–327
6. L. Zhang, E.W. Hansen, I. Helland, E. Hinrichsen, Å. Larsen, J. Roots, Crystallinity in ethene–1-hexene copolymers determined by 1H and 13C NMR. A comparative study. Macromolecules **42**(14), 5189–5195 (2009)
7. B. Blümich, Low-field and benchtop NMR. J. Magn. Reson. **306**, 27–35 (2019)
8. D. Besghini, M. Mauri, R. Simonutti, Time domain NMR in polymer science: from the laboratory to the industry. Appl. Sci. **9**(9), 1801 (2019)
9. E.W. Hansen, P.E. Kristiansen, B. Pedersen, Crystallinity of polyethylene derived from solid-state proton NMR free induction decay. J. Phys. Chem. B **102**(28), 5444–5450 (1998)
10. R. Bärenwald, Y. Champouret, K. Saalwächter, K. Schäler, Determination of chain flip rates in poly (ethylene) crystallites by solid-state low-field 1H NMR for two different sample morphologies. J. Phys. Chem. B **116**(43), 13089–13097 (2012)
11. M. B. Priestley, *Spectral analysis and time series: probability and mathematical statistics* (no. 04; QA280, P7.) (1981)
12. V. Räntzsch et al., Polymer crystallinity and crystallization kinetics via benchtop 1H NMR relaxometry: revisited method, data analysis, and experiments on common polymers. Polymer **145**, 162–173 (2018)
13. E.W. Hansen, X. Gong, Q. Chen, Compressed exponential response function arising from a continuous distribution of gaussian decays-distribution characteristics. Macromol. Chem. Phys. **214**(7), 844–852 (2013)
14. D. Johnston, Stretched exponential relaxation arising from a continuous sum of exponential decays. Phys. Rev. B **74**(18), 184430 (2006)
15. G.E. Pake, Nuclear resonance absorption in hydrated crystals: fine structure of the proton line. J. Chem. Phys. **16**(4), 327–336 (1948)
16. A. Abragam, *The principles of nuclear magnetism (no. 32)* (Oxford University Press, Oxford, 1961)
17. L. Zhang, Z. Liu, Q. Chen, E. Hansen, Quantitative determination of phase content in multiphase polymers by combining spin-diffusion and CP-MAS NMR. Macromolecules **40**(15), 5411–5419 (2007)

18. M. Goldman, L. Shen, Spin-spin relaxation in La F 3. Phys. Rev. **144**(1), 321 (1966)
19. H. Uehara, T. Aoike, T. Yamanobe, T. Komoto, Solid-state 1H NMR relaxation analysis of ultrahigh molecular weight polyethylene reactor powder. Macromolecules **35**(7), 2640–2647 (2002)